

A scalable single-photon imager using a single superconducting nanowire

Authors: Qing-Yuan Zhao¹, Di Zhu¹, Niccolò Calandri^{1,2}, Andrew E. Dane¹, Adam N. McCaughan¹, Francesco Bellei¹, Hao-Zhu Wang¹, Daniel F. Santavicca³, Karl K. Berggren^{1*}

Affiliations:

¹Massachusetts Institute of Technology, Department of Electrical Engineering and Computer Science, Cambridge, MA, 02139

²Politecnico di Milano, Department of Electronics, Information and Bioengineering, Milano, ITA, 22020

³University of North Florida, Department of Physics, Jacksonville, FL 32224

*Correspondence to: berggren@mit.edu

Abstract: Detecting spatial and temporal information of individual photons is a crucial technology and requires advanced single-photon detector (SPD) arrays. Among the current SPDs, detectors based on superconducting nanowires have been demonstrated with outstanding detection performance, but are limited in offering a large-scale array due to the difficulties of cryogenic readout. Here, we demonstrate a scalable single-photon imager using a single continuous photon-sensitive superconducting nanowire, which is designed into a transmission line of ultraslow velocity for electromagnetic waves. Without any multiplexing circuits, the nanowire naturally encodes the spatial and temporal information of a photon on the electrical output pulses. With two readout lines, we are able to resolve ~590 effective pixels and simultaneously obtain a temporal resolution of 50 ps. The performance of the nanowire

imager shows immediate applications in quantum information science, biological imaging and astronomical observation.

One Sentence Summary: After dramatically slowing down the propagation of EM waves, a single nanowire is able to act as a scalable single-photon imager with high spatial and temporal resolution.

Main Text:

Quantum and classical optics are limited by the ability to efficiently sense and process information about single photons. For instance, to enhance the information-carrying capacity of a quantum channel(1) and improve security in quantum key distribution(2, 3), information is encoded on photons in multiple dimensions, requiring detection of photons both in time and space. Determining the spatial and temporal information of photons is currently accomplished by single-photon detector (SPD) arrays. Among existing SPD arrays, the transition edge sensor (TES) and the microwave kinetic inductance detector (MKID) provide excellent spectral information but less impressive temporal resolution (e.g., the timing jitter is ns for TESs(4) and μ s for MKIDs(5)). Photomultiplier tubes and single-photon avalanche diodes have sub-ns timing jitter in the visible domain, but their detection performance deteriorates in the infrared and scaling these technologies to large spatial arrays is challenging(6). Improved timing performance of sub-20-ps timing jitter(7) and sub-10-ns recovery time(8) is possible with superconducting nanowire single-photon detectors (SNSPDs), which also have been demonstrated to have near-unity detection efficiency (9), <1 dark count per second(10), a wide response spectrum from the visible to infrared(11) and >100 MHz counting rate(12). However,

attempts to create arrayed SNSPDs have had limited success(13–18). Traditional row-column rectangular pixel arrays require large numbers of readout lines and precise fabrication tolerance(15), while attempts at time-based and frequency-based multiplexing architectures requiring additional components with pixels suffer from poor fill factors(16, 18). As a result, the current state-of-the-art SNSPD array is limited to 64 pixels.

Rather than developing multiplexing circuits to scale up the number of pixels in an SNSPD array, we add spatial sensitivity to a single superconducting nanowire to let it behave as an imager. The typical operation of an SNSPD lacks spatial sensitivity, although the excitation due to the absorption of a photon is localized within the nanowire. In the phenomenological detection model of an SNSPD(19), an absorbed photon generates a localized region of elevated electron temperature, i.e., a hotspot, which grows to create a resistive domain. Localized photon detection is the fundamental prerequisite for supporting the goal of a spatially sensitive nanowire for imaging. The hotspot scenario indicates that the photon landing location can be well defined by the center of the resistive domain. Unfortunately, the conventional electrical measurement of an SNSPD's output cannot tell us the location of the resistive domain because the nanowire in an SNSPD behaves electrically as a lumped inductor in series with a non-linear resistor that represents the resistive domain(20). In this measurement scheme, the location of the serial resistor in the inductor does not change the output behavior of the lumped circuit model. Therefore, the existing strategies take SNSPDs as discrete detectors and integrate them into an array to gain spatial sensitivity.

Here, we preserve the spatial and temporal information of photon detection events on the electrical measurements after modifying a single superconducting nanowire into a distributed transmission line. This transforms a photon-sensitive nanowire into a scalable single photon imager, which we refer to as a superconducting nanowire single-photon imager (SNSPI) to distinguish it from an SNSPD. The large spatial scalability is attributed to the high kinetic inductance existing in the thin and narrow superconducting nanowire, which slows down the propagation velocity of electromagnetic waves to 2% of the speed of light(21, 22). The spatial and temporal information of photons are extracted from the arrival times of the output pulses. As shown in Fig. 1a, after a photon is absorbed at location x_p at time t_p , the increase of the local resistance generates two electrical pulses of opposite polarities, which propagate with a constant velocity v towards the two ends with delays τ_1 and τ_2 , respectively. By extracting τ_1 and τ_2 from the arrival times of the electrical pulses after removing the fixed delays from tapers, cables and readout electronics, every (x_p, t_p) pair can be mapped out from (τ_1, τ_2) with two linear functions: $x_p = \frac{(\tau_2 - \tau_1)v + L}{2}$ and $t_p = \frac{(\tau_2 + \tau_1) - L/v}{2}$. Such a delay-based readout is similar to a timing-multiplexing architecture for SNSPD arrays(16) or the charge-coupled device (CCD) in which electrical charges are moved out in sequence(23); however, the SNSPI both acts as the detector and intrinsically delays the electrical pulses without any multiplexing circuits or clock signals, resulting in a dramatically compact design that is suitable for large-scale integration. As the nanowire has photon sensitivity along its entire length, photons are able to be sensed continuously along the lateral direction.

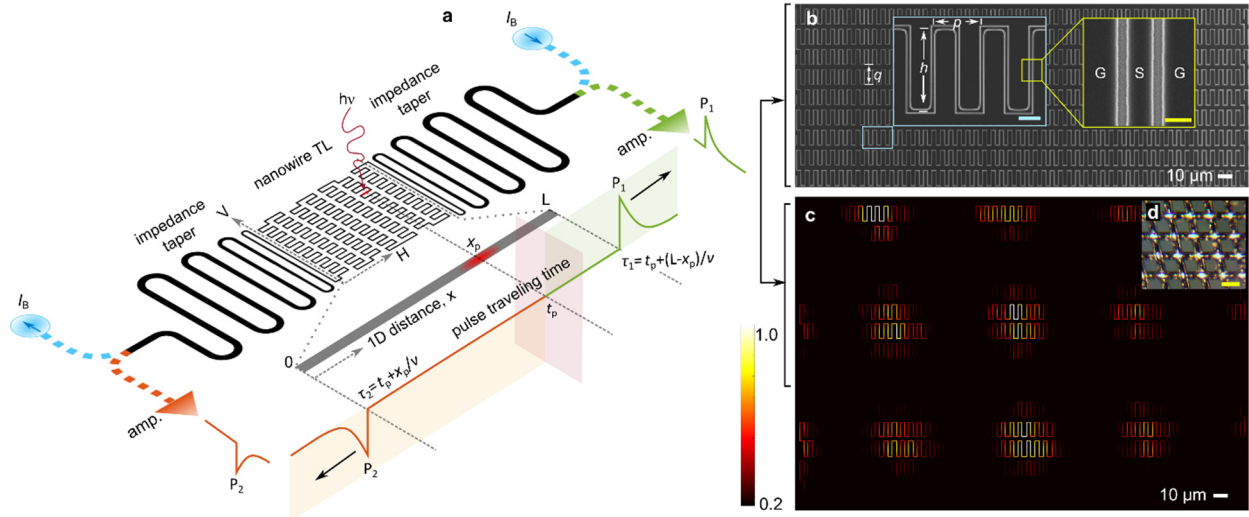


Figure 1 | Superconducting nanowire single-photon imager (SNSPI). **a**, Architecture concept of the SNSPI. The nanowire transmission line (TL) and the impedance tapers are fabricated in coplanar-waveguide structures, where the ground plane is not shown in the sketch. The SNSPI is biased at a constant current I_B and read out by room-temperature amplifiers (amp.). When a photon is absorbed, two pulses propagate towards the nanowire's two ends with delays τ_1 and τ_2 , from which the photon landing location and the photon arrival time can be determined simultaneously. **b**, A scanning-electron-microscopy image of the top nine rows (out of 15 rows in total) of the SNSPI that are meandered from a single 19.7-mm-long nanowire over an active imaging area of $286 \mu\text{m} \times 193 \mu\text{m}$. The dimensions are $q = 13.0 \mu\text{m}$, $h = 9.7 \mu\text{m}$, and $p = 5.4 \mu\text{m}$. The scale bars in the inset figures are $2 \mu\text{m}$ (left) and 300nm (right). **c**, A single-photon image of the pattern formed by light passing through a metal mesh, which is on top of the SNSPI with a gap of $\sim 200 \mu\text{m}$ (see Methods). The circular periodic patterns reflect the opening holes of the mesh. The wavelength of the light is 780nm . The image contains 427,905 photon detections. The color of the map shows the normalized photon counts at each location. **d**, An optical image of the metal mesh, whose opening size is $43 \mu\text{m}$ and wire diameter is $30 \mu\text{m}$. The scale bar is $50 \mu\text{m}$.

To create a 2D image with horizontal and vertical addresses (H, V), the 1D nanowire is folded into a 2D shape. Adjusting the folding geometry will tune the spatial resolution in two directions to meet a particular application (e.g., near field imaging of sub-wavelength resolution with reducing the spacing between adjacent sections of the nanowire). In our experiments, as shown in Fig. 1b, the nanowire is meandered in both the H direction and the V direction to have nearly equal spatial resolution in H and V . This double-meandered nanowire covers a

rectangular area of $286 \mu\text{m} \times 193 \mu\text{m}$. To demonstrate the imaging process, we place an object on top of this rectangular area and evenly illuminate photons through it to project a pattern on the nanowire (see Methods). Figure 1c shows an image of a metal mesh of a simple periodic structure, whose opening holes correspond to the circular patterns of bright colors formed in multiple lines. Figure 2 shows the image construction from detection of 989,897 photons. A video also demonstrates how the accumulation of detection events generates an image, which gives an explicit impression of how the quality of an image is affected by the number of photon detection events (see the Supplementary Video).

The SNSPI's spatial resolution is dominated by the electrical noise in the readout circuits and the speed of signal propagation in the transmission line, rather than by the spatial variation from photon absorption and hotspot dynamics. A photon arriving at x_p will result in pulses observed at times τ_1 and τ_2 . Even if photons hit the same location in the nanowire, the electrical noise will contribute variations in determining τ_1 and τ_2 , resulting in a variation of measured x_p based on the converting function $x_p = \frac{(\tau_2 - \tau_1)v + L}{2}$. We account for this uncertainty by defining a Gaussian blur function $b(x) = e^{-\frac{x^2}{2h^2}}$, where $h = \frac{\delta}{\rho} \times v/2$ (δ is the amplitude of the electrical noise and ρ is the slope of the pulses at the discrimination threshold level). From the waveform of the output pulses, $\frac{\delta}{\rho}$ is measured to be 3.2 ps in our current setup (see Methods). Given this constraint, a slow v can help to reduce h so that the original location of a photon detection event can be determined with less error. For superconducting transmission lines, the existence of the kinetic inductance gives rise to a significant increase in the overall inductance of the

transmission line relative to normal metal lines, resulting in a corresponding reduction of velocity $v = \frac{1}{\sqrt{L_m C_m}}$ (where L_m and C_m are the inductance and capacitance per unit length)(21).

In the SNSPI, as the superconducting nanowire's thickness is much less than the London penetration depth, the kinetic inductance of the nanowire is higher than the geometric inductance by about 2 orders of magnitude (see Methods for the calculation of kinetic inductance and geometric inductance) (22, 24). Additionally, we reduce the gap between the ground and signal line to 100 nm to increase C_m . As a result, the final v is slowed down to 2% of the speed of light c (5.56 $\mu\text{m}/\text{ps}$). Substituting the measured value of v into the blur function $b(x)$, we have $h = 8.9 \mu\text{m}$ and the full-width-at-half-magnitude of $b(x)$ $f_w = 20.9 \mu\text{m}$. The width of $b(x)$ determines the spatial resolution, which will be compared with the measured width of the sharp peaks generated from dark counts in the later discussion.

With the given blur function, the 2D spatial resolution can be calculated by taking into account the meander geometry, from which the 1D distance x is mapped to the 2D location (H,V) . In the geometry shown in Fig 1b, the vertical spatial resolution is the spacing between rows $q = 13.0 \mu\text{m}$ and the horizontal spatial resolution is $f_w \times p/l_m = 5.6 \mu\text{m}$, where $l_m = 22.84 \mu\text{m}$ is the effective length of one meander period in each row. With these high spatial resolutions, we were able to image letters with a 12.6 μm stroke width and 12.6 μm spacing between strokes (see Fig. 2d). A smaller h can be achieved by reducing the timing uncertainty j_e or slowing down v even further by using other superconducting materials of higher kinetic inductance (e.g., tungsten silicide), substrates of higher dielectric constant (e.g., LaAlO_3), or other transmission line structures (e.g., microstrip lines).

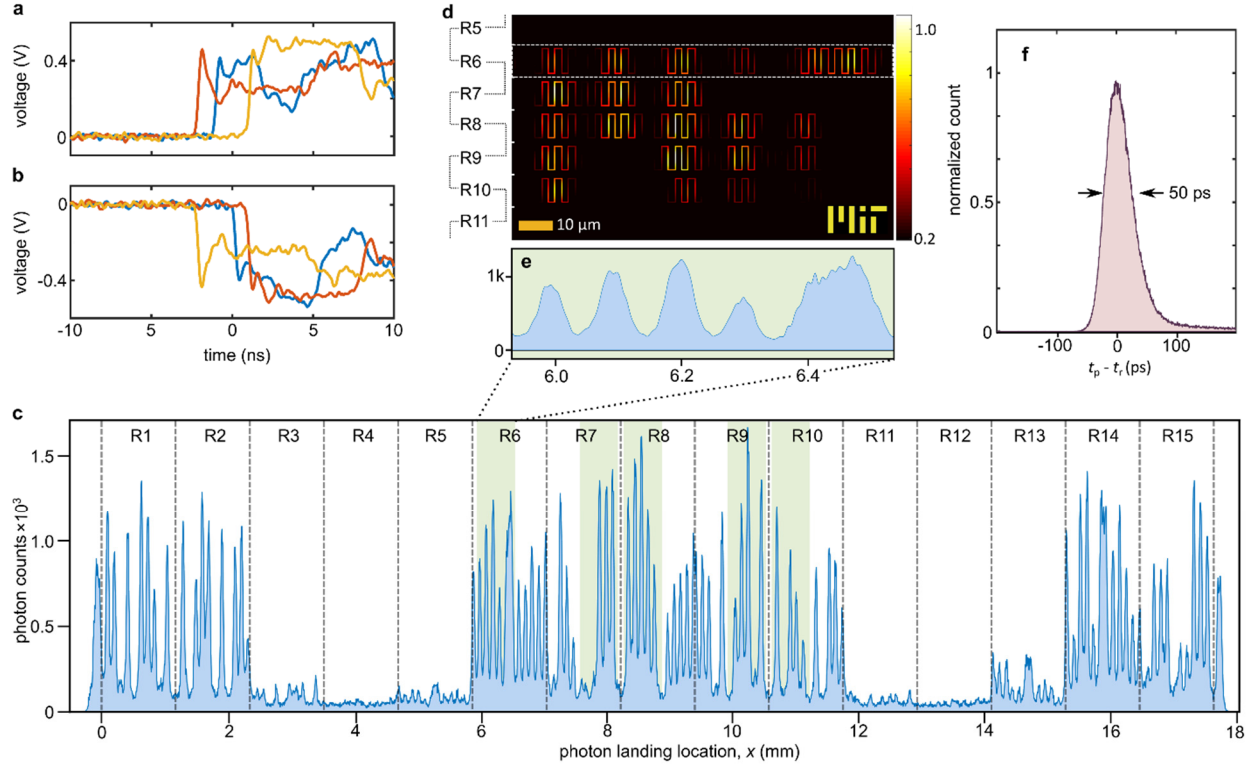


Figure 2 | Spatial and temporal detections by the SNSPI. a, and b, Oscilloscope waveforms of output pulses from the two ends of the nanowire from three photon detections at different locations. We illuminated the device with sub-ps optical pulses from a 1.5 μm mode-locked laser and determined τ_1 and τ_2 with removing the fixed delays outside of the nanowire from the measured arrival times of the pulses. **c,** Histogram of 989,897 photon detections along the 1D distance x . We used a 405 nm light-emitting diode source to project an array of rectangular shapes to minimize the light diffraction, which raises the noise floor for peaks that are close to each other. Timing reference is not necessary for spatial mapping. We read the timing difference of the arrival times to extract $\tau_2 - \tau_1$. The span of x is divided into 15 sections corresponding to the 15 rows of the double-meandered nanowire. **d,** An institutional logo constructed from the peaks covered with green background in the histogram. **e,** The five peaks corresponding to the bright lines included within a white box in row 6. **f.** Histogram of the difference between the photon arrival time t_p measured by the SNSPI and the reference time t_r . We used a 1.5 μm mode-locked laser to illuminate the SNSPI and generate t_r with ps resolution. The FWHM of the histogram profile was 50 ps, which was used for defining the timing jitter j_d .

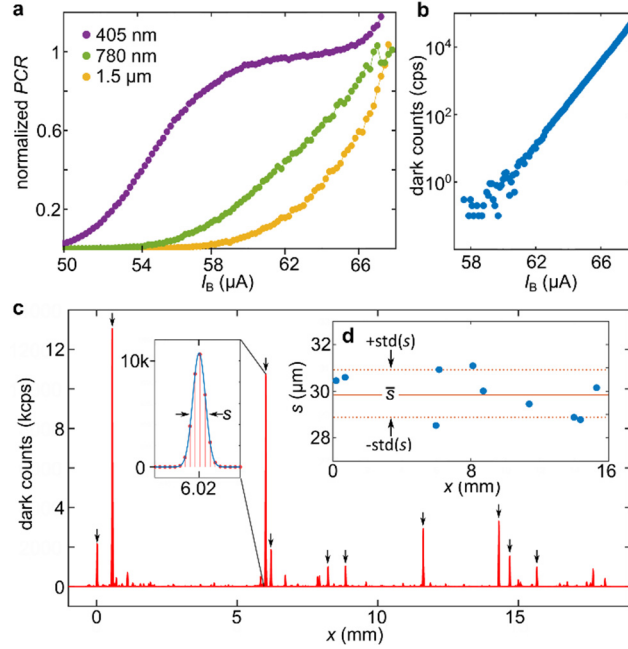


Figure 3 | Detection performance of the SNSPI. **a**, Normalized photon count rate (*PCR*) versus the bias current at wavelengths from visible to infrared. **b**, Overall dark counts versus bias current. **c**, Dark counts histogram over the 1D distance at a bias current of 65 μA . We selected ten peaks of highest amplitude (indicated by the arrows on top) and fit each of them with a Gaussian function, whose FWHM s is calculated. **d**, Distribution of s from the ten peaks. The average of s is $\bar{s} = 29.9 \mu\text{m}$ and the standard deviation is $\text{std}(s) = 0.9 \mu\text{m}$.

Photon arrival time t_p can be measured from $t_p = \frac{(\tau_2 + \tau_1) - L/v}{2}$, which is independent to the measurement of location x_p . The temporal resolution is characterized by the timing jitter j_d , which is defined as the time variation of the measured photon arrival times. To precisely measure j_d , we used a 1.5 μm mode-locked laser, whose output is split into two beams. One beam was sent to the SNSPI for measuring t_p while the other beam was measured by a fast photodiode for supporting a timing reference t_r of ps resolution. Figure 2f shows the histogram of $t_p - t_r$. The FWHM of the histogram profile gives the timing jitter, which is $j_d = 50 \text{ ps}$. This value is within the reported timing jitters for SNSPDs and is significantly lower than the timing

jitters of TESs and MKIDs. Besides the high temporal resolution, the SNSPI also inherits other excellent detection characteristics of an SNSPD, such as high detection efficiency, low dark counts, and wide response spectrum. Figure 3a shows the photon counts versus bias current at wavelengths of 405 nm, 780 nm and 1.5 μm . At 405nm wavelength the internal quantum efficiency of the wire saturates, indicating a near unity internal quantum efficiency of the nanowire. At longer wavelengths, the quantum efficiency is reduced, as would be expected for wires that are 300nm wide. Reducing the wire width, removing the ground plane by using microstrip lines, and integrating an optical cavity will increase the device efficiency for a particular application.

The dark counts of the SNSPI would be a concern for having images of high signal-to-noise-ratio. As shown in Fig. 3b, the dark counts summed over the length of the SNSPI show an exponential increase with bias current, similar to what is measured in SNSPDs. We operated the SNSPI at 60 μA for taking images, where the overall dark counts are about 1 per second, ensuring a high signal-to-noise ratio of the image. To investigate the distribution of dark counts along the nanowire, we increased the bias current to 65 μA to have more dark counts to reduce the overall acquisition time. Figure 3c shows the dark count histogram along the nanowire. We picked up ten peaks of the highest amplitude and calculated the FWHM s for each peak. The average value of s is $\bar{s} = 29.9 \mu\text{m}$ and the variation (defined as the standard deviation) is $\text{std}(s) = 0.9 \mu\text{m}$. Those ten peaks contribute to 74% of the total dark counts, while the overall length is only 2% of the total length of the nanowire, indicating that the image quality is robust to dark counts.

The widths of the dark count peaks are slightly larger than the spatial resolution calculated from the blur function, which might imply the intrinsic length of the dark count locations. To estimate the number of resolvable locations in the SNSPI, we used the measured \bar{s} as the minimum length that the SNSPI was able to distinguish, assuming the locations for generating dark counts and detection photons are equally localized. With these assumptions, the maximum resolvable number of pixels N_p in the SNSPI is $N_p = L/\bar{s} \cong 590$, where $L = 17.635$ mm is the effective length of a straight wire converted from the double-meandered geometry, taking into account the corner geometry.

In summary, we have introduced a scalable architecture for single-photon imagers. By engineering the microwave behavior of a photon-sensitive nanowire into a transmission line with a surprisingly slow velocity of 2% of the speed of light, we have demonstrated ~ 590 effective pixels, sub-20 μm spatial resolution and 50 ps temporal resolution in a 19 mm long superconducting nanowire. To implement SNSPIs into future applications, the microwave design of the nanowire can be combined with optical structures, such as an optical cavity, to enhance the device detection efficiency. Due to the less requirements for readout lines, by integrating many SNSPIs into a super-array, we envision megapixel imagers with GHz counting rate. In addition, the image quality can be further enhanced through improved optics used to focus the object image and superior electronics with less noise and faster acquisition speed. With these improvements, we expect the SNSPI will be used as a powerful single-photon detection tool in various fields, such as quantum information science, single-photon imaging & spectroscopy, and astronomy observation.

References

1. L. Zhang, C. Silberhorn, I. A. Walmsley, Secure quantum key distribution using continuous variables of single photons. *Phys. Rev. Lett.* **100**, 1–4 (2008).
2. S. P. Walborn, D. S. Lemelle, M. P. Almeida, P. H. S. Ribeiro, Quantum key distribution with higher-order alphabets using spatially encoded qudits. *Phys. Rev. Lett.* **96**, 1–4 (2006).
3. M. Mirhosseini *et al.*, High-dimensional quantum cryptography with twisted light. *New J. Phys.* **17**, 1–12 (2015).
4. A. Lamas-Linares *et al.*, Transition edge sensors with low timing jitter at 1550 nm. *Lasers Electro-Optics (CLEO), 2012 Conf.* , 1–2 (2012).
5. J. Gao *et al.*, A titanium-nitride near-infrared kinetic inductance photon-counting detector and its anomalous electrodynamics. *Appl. Phys. Lett.* **101** (2012), doi:10.1063/1.4756916.
6. R. H. Hadfield, Single-photon detectors for optical quantum information applications. *Nat. Photonics.* **3**, 696–705 (2009).
7. L. You *et al.*, Jitter analysis of a superconducting nanowire single photon detector. *AIP Adv.* **3**, 072135 (2013).
8. A. J. Kerman, D. Rosenberg, R. J. Molnar, E. A. Dauler, Readout of superconducting nanowire single-photon detectors at high count rates. *J. Appl. Phys.* **113**, 144511 (2013).
9. F. Marsili *et al.*, Detecting single infrared photons with 93% system efficiency. *Nat. Photonics.* **7**, 210–214 (2013).
10. X. Yang *et al.*, Superconducting nanowire single photon detector with on-chip bandpass filter. *Opt. Express.* **22**, 16267 (2014).
11. F. Marsili *et al.*, Efficient single photon detection from 500 nm to 5 μm wavelength. *Nano Lett.* **12**, 4799–804 (2012).
12. D. Rosenberg, A. J. Kerman, R. J. Molnar, E. A. Dauler, High-speed and high-efficiency superconducting nanowire single photon detector array. *Opt. Express.* **21**, 1440 (2013).
13. Q. Zhao *et al.*, Superconducting-nanowire single-photon-detector linear array. *Appl. Phys. Lett.* **103**, 142602 (2013).
14. S. Miki, T. Yamashita, Z. Wang, H. Terai, A 64-pixel NbTiN superconducting nanowire single-photon detector array for spatially resolved photon detection. *Opt. Express.* **22**, 7811–20 (2014).
15. M. S. Allman *et al.*, A near-infrared 64-pixel superconducting nanowire single photon detector array with integrated multiplexed readout. *Appl. Phys. Lett.* **106**, 192601 (2015).
16. M. Hofherr *et al.*, Time-tagged multiplexing of serially biased superconducting nanowire single-photon detectors. *IEEE Trans. Appl. Supercond.* **23** (2013),

doi:10.1109/TASC.2013.2245935.

17. M. Hofherr *et al.*, Orthogonal sequencing multiplexer for superconducting nanowire single-photon detectors with RSFQ electronics readout circuit. *Opt. Express*. **20**, 28683 (2012).
18. S. Doerner, A. Kuzmin, S. Wuensch, K. Ilin, M. Siegel, Operation of Superconducting Nanowire Single-Photon Detectors embedded in lumped-element resonant circuits. *IEEE Trans. Appl. Supercond.* **PP**, 1–1 (2016).
19. G. N. Gol'tsman *et al.*, Picosecond superconducting single-photon optical detector. *Appl. Phys. Lett.* **79**, 705 (2001).
20. J. K. W. Yang *et al.*, Modeling the Electrical and Thermal Response of Superconducting Nanowire Single-Photon Detectors. *IEEE Trans. Appl. Supercond.* **17**, 581–585 (2007).
21. J. Pond, J. Claassen, W. Carter, Kinetic inductance microstrip delay lines. *IEEE Trans. Magn.* **23**, 903–906 (1987).
22. D. F. Santavicca, J. K. Adams, L. E. Grant, A. N. McCaughan, K. K. Berggren, Microwave dynamics of high aspect ratio superconducting nanowires studied using self-resonance (available at <http://arxiv.org/abs/1602.06895>).
23. W. S. Boyle, G. E. Smith, Charge Coupled Semiconductor Devices. *Bell Syst. Tech. J.* **49**, 587–593 (1970).
24. J. Clem, V. Kogan, Kinetic impedance and depairing in thin and narrow superconducting films. *Phys. Rev. B.* **86**, 174521 (2012).

Acknowledgements

The authors thank Richard Hobbs, Chung-Soo Kim and Mark Mondol for their technical support in nanofabrication, and Philip Mauskopf, Zheshen Zhang and Emily Toomey for scientific discussion. This research was supported by the National Science Foundation (NSF) grants under contract No. ECCS-1509486 (MIT) and No. ECCS-1509253 (UNF), and the Air Force Office of Scientific Research (AFOSR) grant under contract No. FA9550-14-1-0052. Di Zhu is supported by National Science Scholarship from A*STAR, Singapore. Andrew Dane was supported by NASA Space Technology Research Fellowship (award number NNX14AL48H). Adam McCaughan was supported by a fellowship from the NSF iQuISE program (award number 0801525).

Author Contributions

Q.-Y. Z. and K. B. came with the initial idea. Q.-Y. Z. designed and fabricated the nanowire devices. Q.-Y. Z. and D. Z. took the optical measurements. Q.-Y. Z., N.C., F.B., and H.-Z. W. characterized initial devices. A. D. supported the superconducting films. Q.-Y. Z., A.M., and D. S. did the microwave simulations. Q.-Y. Z. analyzed the data and programmed the imaging script. K. B. supervised the project. Q.-Y. Z. and K. B. wrote the paper with input from all other authors.

Methods

Device fabrication and imaging pattern preparation

Device fabrication: The SNSPI was fabricated from a ~7 nm thick niobium nitride (NbN) thin film. The film was deposited on a 4-inch silicon wafer with a 300 nm thick surface layer of silicon dioxide. The NbN had a critical temperature of $T_c = 10$ K, a sheet resistance of $R_s = 331$ Ω /square, and a residual resistance ratio of $RRR = 0.8$. The kinetic inductance was $L_K =$

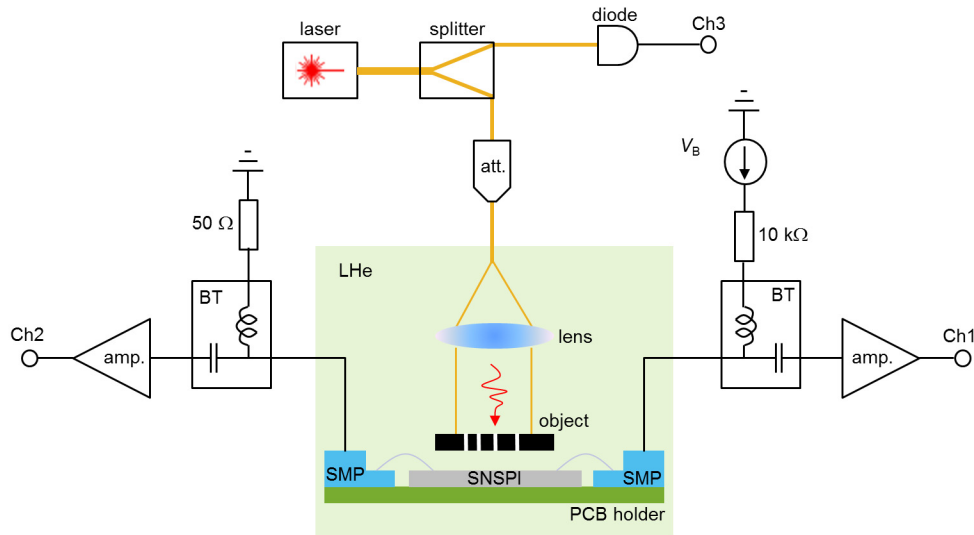
$$\frac{h \cdot R_s}{2 \cdot \pi^2 \cdot \Delta \cdot \tanh\left(\frac{\Delta}{2 \cdot k_B \cdot T_c}\right)} = 49 \text{ pH/square, where } \Delta = 1.76 \cdot k_B \cdot T_c \cdot \tanh\left(1.74 \cdot \sqrt{\frac{T_c}{T} - 1}\right)$$

is the temperature-dependent superconducting energy gap, h is the Planck constant, k_B is the Boltzmann constant, and $T_c = 4.2$ K is the operating temperature(25). The structure of the nanowire transmission line and the tapers was patterned by a 125 kV electron beam lithography tool and then transferred into the NbN layer in a CF_4 atmosphere using a reactive ion-etcher.

Two objects were imaged with the SNSPI. The object used to generate Fig. 1c was a stainless steel mesh (McMaster-Carr part number 34735K69) with an opening size of 43 μm and a wire diameter of 30 μm . The structure of the MIT logo image (Fig. 2d) was patterned by photo-lithography from a lift-off process on an indium-tin-oxide (ITO) substrate. The letters were made from a bilayer of metals (50 nm thick chromium and 50 nm thick gold). For each measurement, we placed the object on top of the device with a gap of about 200 μm .

Imaging Set-up: Here, we give the details of the electrical readouts and the optical setup for operating the SNSPI for taking images, which was shown in Extended Data Fig. 1. We mounted

the SNSPI and the imaged pattern on a PCB board with two coaxial cables for connecting the device to room-temperature readout electronics. The PCB board was mounted on a 2-inch lens tube which has a lens for collimating the laser beam. The SNSPI, imaged pattern, PCB and the tube were immersed in liquid helium at 4.2 K.



Extended Data Figure 1 | Detailed experimental set-up A detailed description is in the Method section ‘setup’. The abbreviations are: att. (optical attenuation), V_B (bias voltage source), BT (bias tee), amp (RF amplifier), SMP (SMP connector), Ch1~Ch3 (the input channels of an oscilloscope), LHe (liquid helium).

The room-temperature readout circuit was used for supplying the SNSPI with a DC bias current, amplifying the output pulses, and determining the pulse arrival times. We used two bias tees (Mini Circuits ZFBT-6GW+) to separate the DC path and the RF path. As the SNSPI is a two-terminal device, we terminated one bias tee’s DC port with a 50Ω load and connected a voltage source (SRS 928) in series with a $10 \text{ k}\Omega$ resistor to the other bias tee’s DC port. With this configuration, a DC current could go through the nanowire. Each bias tee’s RF ports connected

to two RF amplifiers in series (RFbay LNA-2500 in serial with Mini Circuit ZX60-3018G-S), offering a total gain of 47 dB and a bandwidth of 20 MHz~2.5 GHz. The two outputs were acquired by a 6 GHz real-time oscilloscope (Lecroy Wavepro 760Zi). The oscilloscope was triggered by one of the output channels. The arrival times were recorded in the oscilloscope and then exported to computers for image post processing. To detect the arrival times of the electrical pulse, we set a constant discrimination threshold level on the pulse edges. Due to the existence of voltage noise that changed the amplitude of the pulse, the measured arrival times contained another timing variation, which was defined as the electrical jitter j_e . We calculated $j_e = \delta_n/\rho$ from the measured waveforms of the pulses, where δ_n was the root-mean-square noise in a 20 ns timing duration and ρ was the slew rate at the discrimination threshold level. In our setup, for each channel, j_e was 3.2 ± 0.3 ps.

The light was prepared at room temperature and then illuminated on the device through a single-mode fiber (SMF-28) connecting to the lens tube. We used three light sources at different wavelengths, 405 nm, 780nm and 1.5 μm . The light was attenuated to ensure the device was triggered by a single-photon. The 1.5 μm source was a mode-locked laser (Calmar Laser FPL-02CFF), offering sub-ps wide optical pulses at a repetition rate of 20 MHz. We used this source for characterizing the temporal resolution of the SNSPI. In this measurement, the output of the laser was split into two: one illuminated the imager and the other one was detected by a fast photodiode (DET08CFC) as a timing reference. The 780 nm light was a continuous-wave laser source (Thorlabs S1FC780), and the 405 nm light was a fiber-coupled

continuous-wave light-emitting diode. When the continuous-wave sources were used, the splitter and photodiode were removed.

Microwave design of the SNSPI

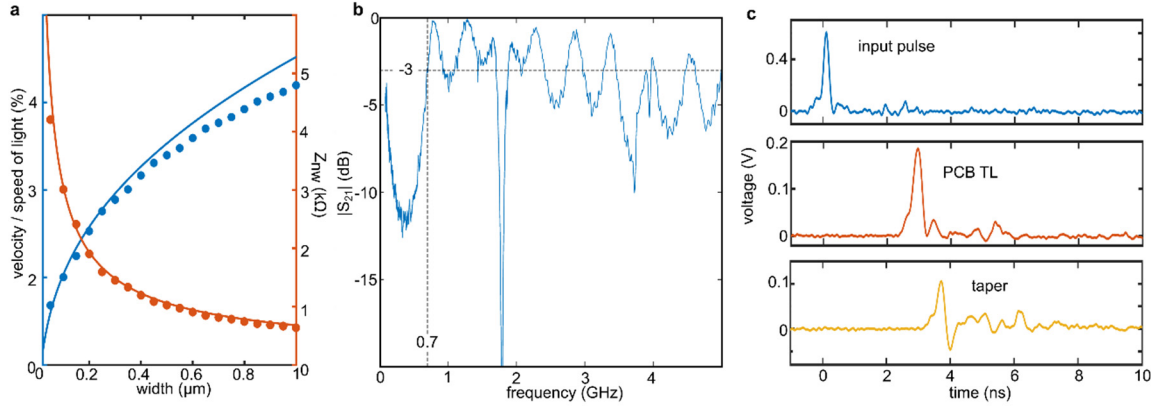
Superconducting kinetic inductance transmission line: We calculated the impedance and velocity of a superconducting transmission line both numerically and analytically. In the analytical calculation, we first calculate the capacitance and inductance of a conventional coplanar waveguide (CPW) made from lossless metal and then replaced the inductance with the total of the kinetic inductance and the geometrical inductance. As shown in Extended Data Fig. 2a, both methods showed similar values.

Wideband impedance transformation by using taper structures: We used the Klopfenstein taper for transforming the nanowire impedance to 50Ω to preserve the fast rising edge of a photon detection pulse(26). In order to verify the taper's performance, we fabricated a 17 mm long NbN taper without a photon-sensitive nanowire at the middle. The taper was designed into a CPW structure with a fixed $3 \mu\text{m}$ gap to the ground plane and a signal line whose width smoothly changed from $88 \mu\text{m}$ at the two ends to $10 \mu\text{m}$ in the center. In order to characterize the superconducting taper without switching it to the normal by the input signals, the narrowest width of the nanowire in the center was designed to $10 \mu\text{m}$ to have a switching current of 0.4 mA.

The bandwidth of the taper was measured by a Network analyzer (see Extended Data Fig. 2b). The pass band of the taper started at 0.7 GHz, which was able to cover the spectrum of the fast edge triggered by photon absorption. The performance of the taper also validated the

calculation of the superconducting transmission line. Although the pass band stopped at 2.4 GHz due to the loss of the PCB board and the bonding wires, the bandwidth was able to support the propagation of a fast pulse.

We demonstrated the pulse propagation by sending a pulse into the taper and measuring the output pulse from the other end. A 200-ps-wide electrical pulse (Avtech, AVMP-2-C-P-EPIA) was split into two. One pulse was acquired by a 6 GHz oscilloscope as a timing reference, while the other pulse was fed into the taper and its transmitted signal was acquired by another channel of the oscilloscope. We also compared the transmitted signal from the taper to the transmitted signal from a 50 Ω transmission line with the same length (corresponding to a delay of 94 ps) but made from a PCB. The delay difference between a PCB transmission line and the taper was 760 ps, indicating the superconducting taper slowed down the average velocity to 11% of a PCB transmission line. The amplitude of the transmitted signal from a taper reduced to 60% of the transmitted signal from the PCB transmission line; however, the rising edge of the pulse was well preserved, verifying that the taper helped the propagation of the fast pulse through a wire of mismatched impedance.



Extended Data Figure 2 | Microwave design of the SNSPI **a**, Calculated velocity and impedance of a superconducting coplanar waveguide at different widths. The dots are from numerical simulation while the lines are from analytical calculation. See Methods for details about the geometry of the wire. **b**, Magnitude of the transmission coefficient $S_{21} = 20 \times \log(V_{\text{out}}/V_{\text{in}})$ of a 17.3-mm-long straight taper without connecting to a photon-sensitive nanowire, where V_{in} is the input signal to the taper from a network analyzer and V_{out} is the output signal through the taper. The high-pass bandwidth starts at 0.7 GHz. The sharp dips close to 2 GHz and 4 GHz are from the wire bonding connections between the chip and the print circuit board (PCB). **c**, Time domain measurement of the taper. We measured the transmitted pulse propagating through the taper and compared it to the transmitted pulse propagating through a 50 Ω PCB transmission line (TL) for evaluating the amplitude loss and the pulse shape distortion of the transmitted pulse propagating through the superconducting taper.

In the SNSPI used for taking images, the taper on each end was designed to have a bandwidth, whose band pass started at 0.8 GHz. Each taper has an overall length of 27 mm, with its width smoothly changing from 105 μm to 300 nm. As shown in Fig. 2a, the rising edge of the photon detection pulses was about 240 ps without any reflection, ensuring the precise measurements of delay times τ_1 and τ_2 .

Imaging processing algorithm

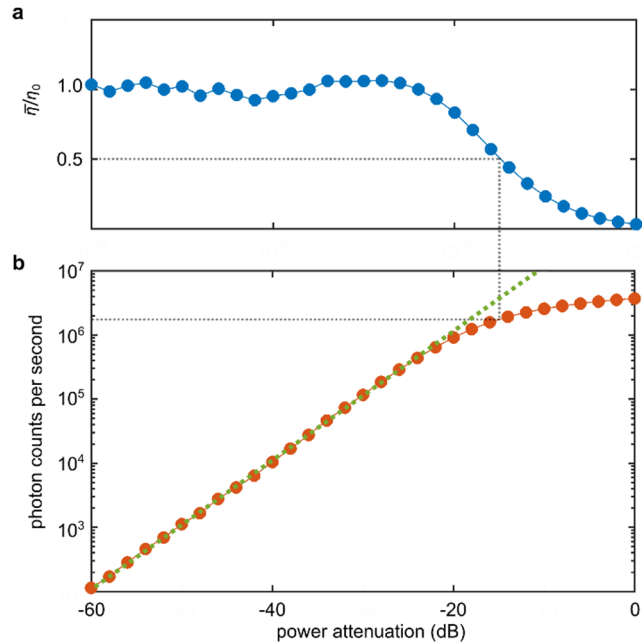
The raw imaging data were derived from the histogram of photon counts over the differential time $\Delta t = \tau_2 - \tau_1$ taken by the oscilloscope. The purpose of the image processing was to map the photon count C_n at each time bin Δt_n to the intensity I_n at the corresponding 2D locations (H_n, V_n) . First, we calculated the effective 1D distance x of the double-meandered nanowire, taking into account the effective length of the corner (the corner's effective length was 0.68 of its physical length) so that we determined a mapping table between x_n and (H_n, V_n) . Secondly, we interpolated the histogram data with a finer time step of 0.045 ps and then converted Δt_n to x_n by $x_n = \frac{\Delta t_n + L}{2}$, where $v = 5.56 \mu\text{m/ps}$ was the velocity and $L = 17.635 \text{ mm}$ was the effective length. Thus, we were able to map the time bin t_n for each photon detection number C_n to the 1D distance x_n . Finally, we set a 2D image frame with grid sizes of $0.5 \mu\text{m}$ in both directions, where the 2D locations (H, V) can be fitted in. For each (H_n, V_n) , the intensity was set to the photon count C_n whose corresponding time bin was t_n and the 1D distance was x_n . To reduce the mapping time, we spread the photon count C_n along the meandered nanowire at (H_n, V_n) in the 2D image, where the photon counts were in a Gaussian function of a standard deviation of $5 \mu\text{m}$. During the mapping process, we shifted Δt to correct for the difference of the delays from electrical connections and adjusted the velocity. The success of the tuning was evaluated by checking the alignments of neighboring rows.

Instead of using the histogram data, the image can be also constructed from compilation of single photon detection events to offer a real-time single-photon video. To use the same image algorithm discussed previously, the raw data was $(\Delta t, 1)$, where each time

difference was assigned to one photon count. The Supplementary Video shows a demonstration of such video by taking the original differential arrival times from the oscilloscope.

Maximum counting rate of the SNSPI

The imaging time was limited by the counting rate of the SNSPI and the acquisition speed of the readout. In our present setup, we used a 6 GHz real-time oscilloscope because of its sub-ps intrinsic timing jitter. However, the oscilloscope had a refresh rate of ~ 100 counts per second, which was the bottleneck that limited the overall imaging time. To investigate the ultimate speed of the SNSPI, we measured the maximum counting rate (CR_{\max}) of the SNSPI, which was defined as the count when the average detection efficiency dropped by a half. As shown in Extended Data Fig. 3, CR_{\max} , was 2 MHz measured for 1.5 μm photons. The measured CR_{\max} indicated the imaging time would reduce to several seconds for taking an image with the same number of photon detection events used for constructing the image shown in Fig.1c or Fig. 2d. The measured CR_{\max} was lower than typical SNSPDs because it had a higher total kinetic inductance (estimated to be $\sim 3 \mu\text{H}$ due to the long wire and the tapers), increasing the time for the bias current in the nanowire to recover⁽⁸⁾.



Extended Data Figure 3 | Maximum counting rate of the SNSPI **a**, The average detection efficiency ($\bar{\eta}$) per second normalized to the detection efficiency for detecting a single photon (η_0) at different attenuations of the incident light. We used a 1.5 μm continuous-wave laser and the readout circuit reported in ref. (27) to avoid the capacitive charging from RF amplifiers. **b**, The photon counts per second versus the attenuation of the incident light. The linear part, shown as the green line, gives η_0 , where the inter arrival time of individual photons is longer than the current recovery time.

References in Methods section

25. A. J. Annunziata *et al.*, Tunable superconducting nanoinductors. *Nanotechnology*. **21**, 445202 (2010).
26. R. Klopfenstein, A Transmission Line Taper of Improved Design. *Proc. IRE*. **44**, 31–35 (1956).
27. Q. Zhao *et al.*, Counting rate enhancements in superconducting nanowire single-photon detectors with improved readout circuits. *Opt. Lett.* **39**, 1869 (2014).